photonics

MDPI

Article

Robust 3D Reconstruction in Turbid Water at Low Sampling Rates via Dual-DMD Single-Pixel System

Wei Feng [1,2,*], Bincheng Wang [1], Xiaoyuan Pan [1], Zhenmin Zhu [3], Shan Lou [2], Dawei Tang [2], Feng Gao [2] and Fumin Zhang [4]

[1] Hubei Key Laboratory of Modern Manufacturing Quality Engineering, School of Mechanical Engineering, Hubei University of Technology, Wuhan 430068, China; wangbincheng@hbut.edu.cn (B.W.); 102410074@hbut.edu.cn (X.P.)
[2] EPSRC Future Metrology Hub, University of Huddersfield, Huddersfield HD1 3DH, UK; s.lou@hud.ac.uk (S.L.); d.tang@hud.ac.uk (D.T.); f.gao@hud.ac.uk (F.G.)
[3] School of Electrical and Electronic Engineering, East China Jiaotong University, Nanchang 330013, China; zhuzhenmin1984@163.com
[4] State Key Laboratory of Precision Measurement Technology and Instruments, Tianjin University, Tianjin 300072, China; zhangfumin@tju.edu.cn
* Correspondence: fengwei@hbut.edu.cn

Abstract

Conventional optical imaging struggles to acquire clear images of underwater scenes in turbid water. In this paper, a new dual-DMD single-pixel 3D imaging (DSP3DI) system is designed and constructed to realize the 3D shape reconstruction in highly turbid water conditions. Leveraging the spectral dependence of the scattering coefficient of water on wavelength, the designed system uses a 532 nm laser as the illumination source to minimize scattering and absorption losses during light propagation, and two digital micromirror devices (DMDs) are used to generate phase-shifting fringe patterns and sampling patterns, respectively, and then uses a single-pixel detector to sequentially collect the spatial light field reflected from the surface of the object. A single-pixel imaging (SPI) method based on a cake-cutting strategy for Hadamard encoding reconstructs the deformed fringe images, from which phase information is recovered to calculate the 3D shape of objects. The experimental results show that the system not only achieves millimeter-level measurement accuracy but also successfully reconstructs the 3D shape of complex objects at a sampling rate of 10% and in turbidities as high as 40 NTU. The proposed system, characterized by its compact structure, high measurement accuracy, and strong scattering resistance, offers a novel solution for high-precision 3D imaging in highly turbid water.

Keywords: single-pixel imaging; 3D reconstruction; structured illumination; dual DMD system; highly turbid water

Check for updates

Received: 31 March 2026
Revised: 22 April 2026
Accepted: 28 April 2026
Published: 1 May 2026

Copyright: © 2026 by the authors. Licensee MDPI, Basel, Switzerland. This article is an open access article distributed under the terms and conditions of the Creative Commons Attribution (CC BY) license.

1. Introduction

Underwater 3D optical imaging technology has great potential for applications in marine science research, underwater archaeology, and ocean engineering [1,2]. Nevertheless, optical imaging in underwater environments, especially in turbid water, remains a formidable challenge. Light propagation in water is subject to strong absorption and scattering, resulting in a significant reduction in the signal-to-noise ratio (SNR) and a severe loss of detail in images captured by conventional cameras, it is difficult to acquire clear and reliable 3D data [3–5]. Therefore, the development of imaging technology capable of

high-precision 3D reconstruction is of significant both theoretical and practical importance in strong scattering environments.

Single-pixel imaging (SPI) provides an effective alternative approach. In an SPI setup, a conventional multipixel detector (such as a CCD or CMOS sensor) is replaced by a single-pixel detector (SPD) devoid of spatial resolution [6]. This system utilizes a spatial light modulator to encode the scene, with the image subsequently reconstructed from a time-series of intensity signals. This unconventional imaging paradigm endows SPI with exceptionally high detection sensitivity and strong scattering resistance [7], so it offers a unique advantage in low-light and highly turbid media [8–10].

Many researchers have explored different approaches to extend SPI from 2D imaging to 3D reconstruction. For example, a fast 3D imaging technique combining time-of-flight measurement with a 2D compressed sensing algorithm was proposed to obtain depth information, but the practical application of conventional methods was limited by the slow convergence speed of one-dimensional reconstruction algorithms [11]. A spectroscopic 3D SPI system based on virtual binocular vision was proposed to acquire disparity information through a dual-detector setup, but the setup lacked robustness in scattering environments [12]. Photometric stereo techniques utilizing multiple detectors were used to reconstruct surface normals for 3D geometry recovery, but the measurement accuracy was heavily limited by the strict reliance on surface reflection properties and the complexity of the hardware configuration [13]. Although these methods have significantly advanced 3D SPI technology, they still face challenges in simultaneously achieving high measurement accuracy, system robustness, and practical deployment complexity.

Combining fringe projection profilometry (FPP) with SPI has emerged as a promising way for high-precision 3D reconstruction. Early studies incorporated phase-shifting algorithms into SPI systems, validating the feasibility of 3D reconstruction but facing complex system calibration challenges [14]. Fourier transform profilometry method based on 2D discrete cosine transform was proposed to achieve rapid phase recovery through spectral modulation, but it was susceptible to noise in high-frequency components [15]. A Fourier single-pixel imaging (FSPI) method with an optimized sampling strategy was introduced to significantly reduce the sampling rate, but it showed performance degradation in complex scattering media [16]. A pseudo-camera calibration framework was also proposed to greatly improve the calibration accuracy of SPI systems, but its effectiveness relied heavily on the initial pixel-matching accuracy [17]. Despite these advancements, most studies were conducted in air and, thus, fail to address the substantial challenges posed by strong scattering in underwater environments.

Research on applying SPI technology to underwater environments has also made some notable progress. For instance, a Hadamard-encoded SPI system was used to demonstrate scattering-resistant 2D imaging, demonstrating its scattering resistance but failing to acquire 3D information [18]. A laser ghost imaging method based on Walsh speckle patterns was proposed to improve the imaging SNR and scattering resistance by optimizing the encoding structure and laser modulation strategy, but it remained a 2D imaging system [19]. Recently, a comparative study of underwater structured light 3D reconstruction techniques was conducted to analyze performance differences among mainstream methods, but it did not overcome the imaging challenges in highly turbid water [20]. Furthermore, a Fourier single-pixel 3D imaging method based on pseudo-camera calibration achieved good reconstruction results in high turbidity and at low sampling rates [21]. Nevertheless, this method relied on a camera to capture 2D images, which were then spatially integrated to emulate the measurement of an SPD. In contrast, an SPD could directly measure the intensity corresponding to each projected pattern. Moreover, the limited penetration

capability of conventional light sources in turbid water further constrained the application of this system in more severe conditions.

To address these limitations, a new dual-DMD single-pixel 3D imaging system was designed and constructed to reconstruct the 3D shape information in highly turbid water. Two DMDs are used to generate phase-shifting fringe patterns and sampling sequence patterns, respectively, and an SPD is used to sequentially collect the spatial light field reflected from the object surface. The SPI method is then used to reconstruct the deformed fringe images, from which phase information is recovered to compute the 3D shape of objects. The experimental results demonstrate that the proposed system not only achieves millimeter-level measurement accuracy but also successfully reconstructs the 3D shape of complex objects at a sampling rate of 10% and in turbidities as high as 40 NTU. With its compact structure, high measurement accuracy, and strong scattering resistance, the proposed system offers a promising solution for high-precision 3D imaging in highly turbid underwater environments.

The remainder of this paper is organized as follows: Section 2 introduces the principle of the DSP3DI system. Section 3 presents the imaging and calibration methodologies. Section 4 describes the experimental setup and evaluates the fundamental 3D reconstruction accuracy. Section 5 analyzes the system performance in scattering environments. Finally, Section 6 concludes the paper.

2. Approaches

2.1. DSP3DI System Design

The proposed DSP3DI system is shown in the diagram in Figure 1, where the green, yellow, blue, and orange arrows represent the transmitting optical path, receiving optical path, calibration branch, and imaging branch, respectively. The setup consists of the following three main components: illumination, detection, and calibration units. In the illumination path, a 532 nm semiconductor laser first passed through the beam-expanding and collimating lenses (L1 and L2) and was then redirected by a plane mirror (M) onto DMD1. Then the DMD1 modulated the incident beam into the desired fringe patterns, which were projected onto the object surface. This wavelength was selected because it lied in the blue–green spectral window of water, where absorption and scattering were relatively low, thus reducing transmission loss in turbid water [22].

After interacting with the object surface, the reflected light propagated along the receiving path and was collected by lens L3. The collected light was then directed by the total internal reflection (TIR) prism onto DMD2, where the reflected scene was spatially encoded by the preset sampling patterns. After modulation by DMD2, the light passed through the beam splitter (BS) and was focused by lens L4 onto the SPD, which recorded the integrated intensity corresponding to each sampling pattern. For calibration, a portion of the light after the beam splitter was redirected to a high-resolution CMOS camera to form the calibration branch. In this way, the system realized structured-light projection through DMD1 and SPI through DMD2. The measurement object is placed in a water tank, and calcium carbonate powder is added to simulate underwater scattering environments with varying turbidity levels.

The specific design of this system offers three key advantages. First, the dual-DMD setup integrates laser-based active illumination with single-pixel passive detection. DMD1 modulates the laser source into high-intensity structured light patterns, and with the illumination path dedicated to projection, DMD2 is used to spatially encode the reflected light field. This architecture effectively filters backscatter noise. Second, the 532 nm laser source minimizes attenuation in water, enhancing signal strength in turbid conditions.

Finally, the integration of the pseudo-camera calibration unit ensures high geometric accuracy, allowing for precise millimeter-level 3D reconstruction.

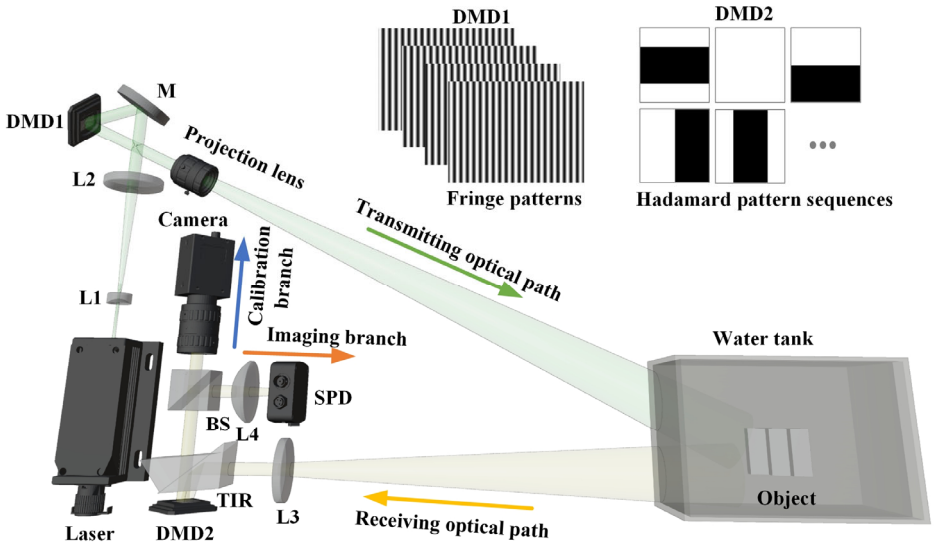


Figure 1. Schematic diagram of DSP3DI system. The green, yellow, blue, and orange arrows represent the transmitting optical path, receiving optical path, calibration branch, and imaging branch, respectively.

2.2. 3D Imaging Principle

The imaging process of the DSP3DI system is summarized in Figure 2, and it includes the following steps:

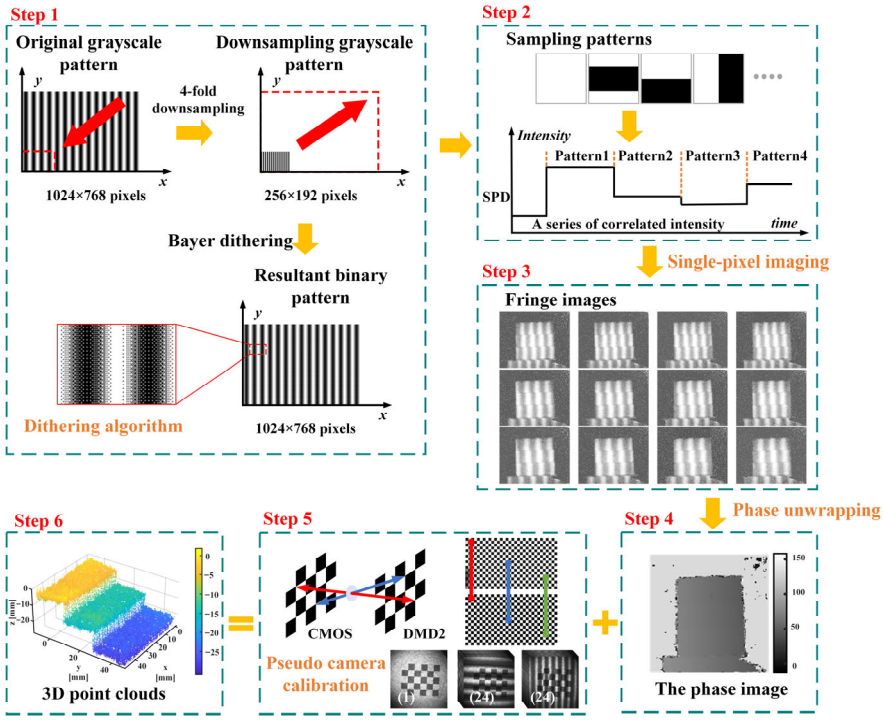


Figure 2. Workflow of the DSP3DI system, including pattern generation, SPI-based reconstruction, phase retrieval, system calibration, and 3D point cloud generation.

Step 1: Fringe projection. Sinusoidal fringe patterns are first generated according to the phase-shifting scheme and then binarized using a dithering algorithm so that they

can be displayed by the DMD. These fringe patterns are projected onto the object surface through DMD1, where the object shape modulates the projected fringes.

Step 2: Information encoding. The deformed light field reflected from the object surface is collected by the detection unit and directed to DMD2. During the acquisition of each deformed fringe image, the fringe pattern projected by DMD1 remains unchanged, while DMD2 sequentially displays a set of predefined sampling patterns to spatially encode the reflected light field. For each sampling pattern, the SPD records the integrated light intensity, thereby converting the two-dimensional optical field into a one-dimensional sequence of correlation measurements for reconstructing that fringe image.

Step 3: 2D image reconstruction. According to the acquired single-pixel measurements and the corresponding sampling patterns, an SPI reconstruction algorithm is used to recover the two-dimensional deformed fringe images [18]. Repeating this process for all projected fringe patterns produces the complete fringe sequences required for phase retrieval.

Step 4: Phase unwrapping. Before phase calculation, each reconstructed fringe image is preprocessed to reduce phase errors, including histogram equalization and Gaussian filtering. The preprocessed multi-step deformed fringe images are then used to calculate the wrapped phase of the object surface by phase-shifting profilometry. A multi-wavelength phase unwrapping method is further applied to obtain the absolute phase distribution, which contains the depth information of the object surface [21].

Step 5: System calibration. To improve the accuracy of 3D reconstruction, an auxiliary CMOS camera and an improved pseudo-camera calibration method are used to determine the intrinsic and extrinsic parameter matrices of both DMD1 and DMD2. This step establishes the geometric mapping between the phase information and the physical coordinates in the measurement space.

Step 6: 3D coordinate calculation. Based on the principle of triangulation, the 3D surface coordinates are derived by integrating the absolute phase with the parameters of system calibration.

3. Methods

3.1. Fringe Projection Based on Dithering Algorithm

In single-pixel 3D imaging, a DMD simulates grayscale by temporally integrating a series of binary bit-plane patterns at high speed. This results in a dynamically changing instantaneous light intensity during the integration period. SPI data acquisition, however, is a time-series measurement process that requires the measured scene to remain static throughout the acquisition of thousands of encoding patterns for a single deformed fringe image [23]. This paper adopts a spatial dithering algorithm to improve the fidelity of sinusoidal fringe generation, which resolves this issue [24]. This algorithm quantizes each pixel of an ideal grayscale image into a binary state using a predefined 2D threshold matrix. The Bayer dithering matrix can be generated by the following recursive formula:

$$\begin{cases} M_1 = \begin{bmatrix} 0 & 2 \\ 3 & 1 \end{bmatrix} \\ M_{k+1} = \begin{bmatrix} 4M_k & 4M_k + 2U_k \\ 4M_k + 3U_k & 4M_k + U_k \end{bmatrix} \end{cases}, \quad (1)$$

where M_1 is the minimal 2×2 base dithering matrix, k is the dimension of the matrix, and U_k is the k-dimensional unit matrix. The binary dithering patterns generated in this manner preserve the macroscopic grayscale distribution characteristics of the original sinusoidal fringes.

A combined downsampling with upsampling dithering method is used to ensure that the local average intensity of the binary patterns accurately represented the original grayscale values. First, the ideal sinusoidal fringe image is downsampled by a factor of four. Subsequently, a matrix, M_2, is used to re-encode this averaged intensity value into a high-resolution 4×4 binary pixel block. This method ensures that the average light intensity of the binary pattern within a local spatial area accurately represented the original grayscale value, thereby better preserving the energy distribution of the low-frequency sine wave.

$$M_2 = \begin{bmatrix} 0 & 8 & 2 & 10 \\ 12 & 4 & 14 & 6 \\ 3 & 11 & 15 & 7 \\ 15 & 7 & 13 & 5 \end{bmatrix},$$

These high-frequency binary dithered patterns were projected by the projector in a slightly defocused state. The defocusing effect of the projection lens blurred the sharp edges of the binary patterns, thereby forming a smooth light-field distribution on the object surface that was macroscopically equivalent to high-quality grayscale sinusoidal fringes.

3.2. Phase Recovery Based on Multi-Wavelength Phase-Shifting Profilometry

In single-pixel 3D imaging, the accurate recovery of the absolute phase is central to achieving 3D reconstruction. This system uses the classic N-step phase-shifting profilometry as the fundamental framework for phase solving [25]. The intensity distribution of the n-th captured deformed fringe image can be expressed as follows:

$$I_n(x, y) = A(x, y) + B(x, y) \cos[\phi(x, y) - 2\pi n/N], n = 1, 2, \cdots, N, \tag{2}$$

where $I_n(x, y)$ denotes the captured intensity at pixel coordinate (x, y) corresponding to the n-th phase shift; n is the phase-shift index; N represents the total number of phase-shifting steps; $A(x, y)$ and $B(x, y)$ are, respectively, the background intensity and amplitude; and $\phi(x, y)$ is the modulated phase containing the depth information of the object surface. By solving the following least-squares problem for N images at each pixel, the wrapped phase $\varphi(x, y)$, confined to the interval $(-\pi, \pi)$, can be calculated as follows:

$$\varphi(x, y) = \arctan \frac{\sum_{n=1}^{N} I_n(x, y) \sin(2\pi n/N)}{\sum_{n=1}^{N} I_n(x, y) \cos(2\pi n/N)}, \tag{3}$$

The wrapped phase $\varphi(x, y)$ is discontinuous. A phase unwrapping algorithm must be used to remove the 2π phase jumps and reconstruct a monotonically increasing continuous phase, known as the absolute phase $\phi(x, y)$.

$$\phi(x, y) = \varphi(x, y) + 2\pi k(x, y), \tag{4}$$

where $k(x, y)$ is the fringe order required to be determined. The core challenge of absolute phase recovery is to quickly and accurately determine k for each pixel in the phase image. A robust temporal phase unwrapping method using multiple wavelengths is adopted. By calculating the difference between two wrapped phases, $\varphi_h(x, y)$ and $\varphi_l(x, y)$, an equivalent, lower-frequency wrapped phase, $\varphi_{eq}(x, y)$, can be generated, as follows:

$$\varphi_{eq}(x, y) = \varphi_h(x, y) - \varphi_l(x, y), \tag{5}$$

$$\lambda_{eq} = \frac{\lambda_l \lambda_h}{\lambda_l - \lambda_h}, \tag{6}$$

where λ_h and λ_l represent the spatial periods of the component fringes. λ_{eq} is also known as the synthetic wavelength. The synthetic phase image, $\varphi_{eq}(x, y)$, is typically used only as a reference phase to aid in phase unwrapping.

$$k_h(x,y) = round[\frac{(\lambda_{eq}/\lambda_h)\varphi_{eq}(x,y) - \varphi_h(x,y)}{2\pi}], \quad (7)$$

where $k_h(x, y)$ is the fringe order required for unwrapping the high-frequency wrapped phase, $\varphi_h(x, y)$. It should be noted that the dual-wavelength temporal phase unwrapping method can be extended to three or even more wavelengths, thereby further increasing the equivalent wavelength.

3.3. High-Precision Geometric Calibration Based on a Pseudo-Camera Framework

Accurate geometric calibration is critical for achieving high-precision 3D reconstruction in SPI systems, and the low-resolution images typically produced in SPI to maintain practical acquisition speeds lead to significant quantization errors when used directly for calibration. To address this issue, the improved pixel-mapping pseudo-camera calibration method proposed by Feng is adopted in this work [20]. DMD2 cannot capture images, and, therefore, a high-resolution CMOS camera is temporarily inserted into the path. DMD2 displays checkerboard patterns, and the auxiliary camera records the corresponding images, from which a precise pixel-to-pixel correspondence between the CMOS sensor and the micromirror array of DMD2 is established through nonlinear polynomial fitting. This process achieves sub-pixel mapping accuracy and enables reliable geometric calibration for subsequent 3D reconstruction.

4. Experiments and Results

4.1. Hardware Implementation

A DSP3DI system was constructed to simulate and study the light propagation characteristics dominated by absorption and scattering effects in underwater environments, as shown in Figure 3, which illustrates the optical paths for pattern projection and signal detection, along with a photograph of the complete system. The experimental setup utilized a dual-DMD architecture that combined active structured light illumination with encoded spatial detection. By decoupling the projection and detection modulations, this configuration effectively suppressed volume scattering noise and significantly enhanced the SNR, thereby enabling the acquisition of robust 3D information in turbid media.

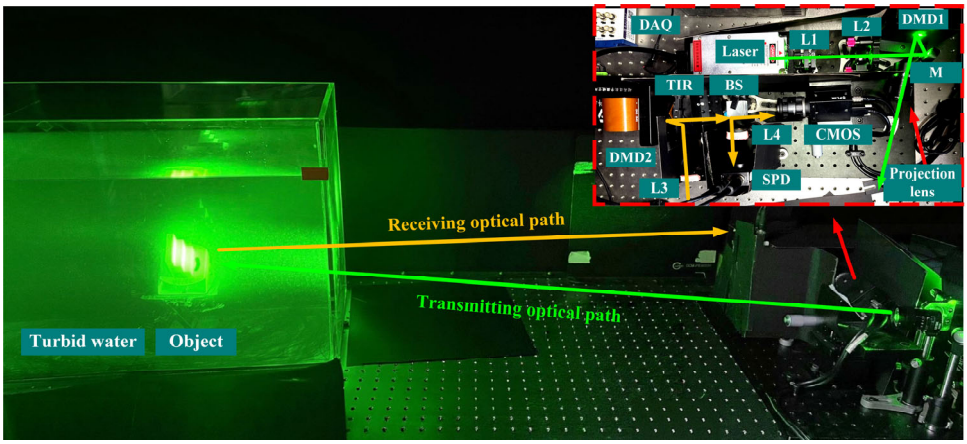


Figure 3. Experimental setup illustrating the optical paths for pattern projection and signal detection, along with a photograph of the complete system.

The light source of the system was a 532 nm semiconductor laser (CNIlaser, Changchun, China, MGL-U-532). The laser beam was expanded and collimated, then directed to DMD1 (Fldiscovery, Jinhua, China, F4320-DDR-0.7-XGA), which projected a preset sequence of sinusoidal patterns onto the surface of the target object. The reflected light field, modulated by the 3D shape of the object surface, was collected by a lens and guided via a total internal reflection prism to DMD2 (Fldiscovery, F4320-DDR-0.96-WUXGA). DMD2 then loaded a preset sequence of specified sampling patterns to spatially encode the light field. The system used a block compressive sensing strategy to improve the SNR. It divided the DMD2 surface into a 128 × 128 grid of macro-pixels, each made of 8 × 8 physical micromirrors, achieving a reconstruction resolution of 128 × 128 pixels. The modulated total light intensity was finally received by an SPD (Newton, NJ, USA, Thorlabs, PDA100A2) and converted into a voltage signal for image reconstruction.

For the calibration system, a high-resolution CMOS camera (Wilsonville, OR, USA, Flir, GS3-U3-32S4M-C) was temporarily added to the system. The entire optical system was built on a 0.3 m × 0.45 m optical breadboard, with a designed working distance of 0.9 m to 1.0 m. The object was placed in a 0.6 m × 0.3 m × 0.5 m water tank. Suspensions of varying turbidity were created by adding specific masses of calcium carbonate ($CaCO_3$) powder to clear water. The turbidity was quantified based on the standard where a 1 mg/L $CaCO_3$ suspension corresponds to 1 NTU [26]. All experiments were conducted in a darkroom to shield the highly sensitive SPD from ambient stray light.

4.2. System Calibration Results

4.2.1. Binarization Algorithm Results

Before formally evaluating the 3D reconstruction performance, it was essential to first validate the effectiveness of the key step of converting ideal sinusoidal fringes into binary patterns suitable for the DMD. An inappropriate binarization algorithm could introduce severe harmonic errors, fundamentally compromising the accuracy of phase measurement.

A Blender-based simulation platform (Blender v3.4.1) was constructed to quantitatively evaluate how different binarization algorithms influence fringe quality [27]. In the simulation, the optical defocus introduced by the projection lens was modeled as a 2D Gaussian low-pass filter [28]. The Bayer dithering algorithm and the Floyd–Steinberg error-diffusion method were compared using this platform.

As shown in Figure 4a–c, the simulation results for the ideal sinusoidal fringe, the Bayer-dithered pattern, and the Floyd–Steinberg pattern were presented, respectively. Each sub-figure contained three columns: the left column showed the deformed fringe image after Gaussian defocusing, the middle column displayed the reconstructed absolute phase map, and the right column illustrated the corresponding projection pattern used in the simulation. A quantitative evaluation was provided in Figure 4d, where the phase map obtained from the ideal sinusoidal fringe in Figure 4a was treated as the ground truth and the reconstruction errors for Figure 4b,c were computed accordingly.

Under identical defocused conditions, a root mean square error (RMSE) of 1.129 rad was obtained using Bayer-dithered patterns, whereas a significantly higher RMSE of 6.806 rad was produced by the Floyd–Steinberg algorithm. This nearly six-fold difference demonstrated that the Bayer dithering algorithm more effectively preserved the fundamental frequency component of the sinusoidal carrier and reduced nonlinear distortion introduced during binarization. Consequently, the Bayer dithering algorithm was selected for the proposed system to achieve high-fidelity phase recovery.

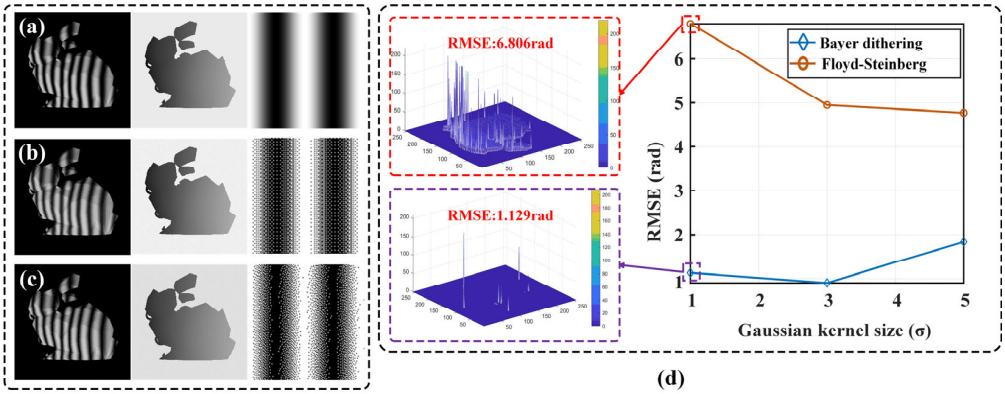


Figure 4. Simulation comparison of Bayer dithering and Floyd–Steinberg dithering algorithms: (**a**) ideal sinusoidal fringe; (**b**) Bayer dithering; (**c**) Floyd–Steinberg dithering; (**d**) comparison of absolute phase RMSE under different Gaussian kernels.

4.2.2. Pixel Mapping and Calibration Results

The primary step in calibration was to perform pixel-level mapping to establish a precise correspondence between the image coordinate system of CMOS camera and the micromirror coordinate system of DMD2. Specifically, the DMD2 surface was first illuminated with uniform white light, and then an 18 × 32 checkerboard pattern was displayed on it. A high-resolution CMOS camera captured this pattern, and the precise coordinates of the checkerboard corners were extracted. Finally, a least-squares method was used to fit the polynomial model, completing the mapping between the two coordinate systems.

As shown in Figure 5, (a) and (d) were the checkerboard corner points and the fitted planes, (b) and (e) presented the fitted residual results in the x and y directions, respectively, and (c) showed the checkerboard image captured by the CMOS camera, whereas (f) showed the corresponding checkerboard pattern displayed on DMD2. In these plots, the green circles denoted the residual values, the vertical lines indicated the confidence interval ranges, and the red markers identified residual outliers—defined as points where the confidence interval excludes zero. The data error at these outliers was relatively large. However, the overall residuals of the fit were within ±0.4 pixels in both directions, which ensured the high quality of the pixel-mapping results.

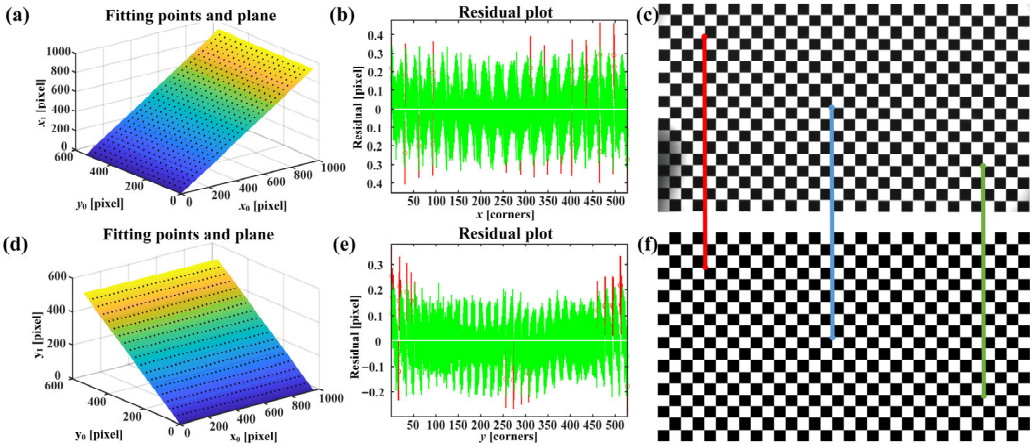


Figure 5. Mapping results: (**a**,**d**) checkerboard corner points and the fitted planes; (**b**,**e**) residuals between the original and fitted corner points; (**c**) checkerboard image captured by the CMOS camera; (**f**) corresponding checkerboard pattern displayed on DMD2.

Figure 6 illustrates the calibration process between DMD1 and DMD2 using three-wavelength phase-shifting profilometry. Horizontal and vertical sinusoidal fringes at

three spatial frequencies of 16, 18, and 21 (period: pixel) were projected onto the circular calibration plane. Due to the limited effective field of view of the imaging system, only the central region of the projected patterns could be obtained, rather than the complete fringe images. As a result, phase information was available only within this region, leading to the incomplete appearance of the synthesized low-frequency wrapped phase.

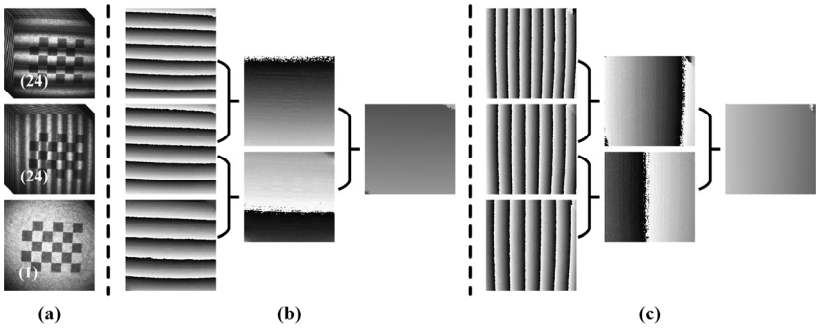


Figure 6. Calibration process using three wavelength phase shift profilometry: (**a**) horizontal and vertical fringe images and checkerboard images for three wavelengths in the CMOS coordinate system; (**b**) and (**c**) unwrapped absolute phases in the horizontal and vertical directions, respectively.

The projection sequence included phase-shifted patterns and checkerboard images, resulting in a total of 49 images. By processing the deformed fringe images captured by the auxiliary camera, the phase distributions of the horizontal and vertical fringes were computed by using the three-wavelength algorithm. By decoding the fringe patterns, the pixel coordinates of the feature points on the virtual image plane of DMD1 were accurately determined. Datasets acquired from multiple poses of the calibration board were jointly used to estimate the geometric relationship between DMD1 and DMD2, from which the intrinsic and extrinsic parameter matrices were obtained [29].

However, the initial calibration was performed at a high resolution (512 × 512 pixels) while the SPI system operated at a lower resolution (128 × 128 pixels), and, thus, a coordinate conversion was necessary to ensure parameter consistency. According to this scaling requirement, a factor $s = 4$ was used to scale the original data.

In Equation (8), K' denoted the rescaled intrinsic matrix, where f_x and f_y represented the focal lengths scaled by the pixel size in the horizontal and vertical directions, respectively, and they served as scaling factors from distance units to pixel units. Meanwhile, c_x and c_y were the coordinates in the pixel coordinate system.

$$K' = \begin{bmatrix} f_x/s & 0 & c_x/s \\ 0 & f_y/s & c_y/s \\ 0 & 0 & 1 \end{bmatrix}, \tag{8}$$

The finalized calibration data were obtained, K_{DMD1} and M_{DMD1} served as the intrinsic and extrinsic matrices for DMD1, while K'_{DMD2} and M'_{DMD2} were the corresponding intrinsic and extrinsic matrices for DMD2.

$$\begin{cases} K_{\mathrm{DMD1}} = \begin{bmatrix} 3947.303 & 0 & 242.820 \\ 0 & 4044.300 & 50.925 \\ 0 & 0 & 1 \end{bmatrix} \\ M_{\mathrm{DMD1}} = \begin{bmatrix} 3807.978 & -127.311 & -1059.838 & 338482.206 \\ -71.091 & -4038.117 & 217.977 & 695842.010 \\ -0.201 & -0.062 & -0.976 & 1227.454 \end{bmatrix}' \end{cases}$$

$$\begin{cases} K'_{\mathrm{DMD2}} = \begin{bmatrix} 1140.683 & 0 & 54.244 \\ 0 & 1133.684 & 63.178 \\ 0 & 0 & 1 \end{bmatrix} \\ M'_{\mathrm{DMD2}} = \begin{bmatrix} -1141.040 & 23.603 & 39.638 & 79625.288 \\ -20.680 & -1123.871 & 160.371 & 72004.556 \\ -0.011 & 0.0861 & 0.996 & 809.106 \end{bmatrix}' \end{cases}$$

4.3. Single-Pixel Reconstruction and 3D Measurement Accuracy

In single-pixel 3D imaging systems, acquiring high-quality deformed fringe images was a prerequisite for accurate phase unwrapping and 3D reconstruction. However, the laser source utilized in this system introduced speckle effects, which reduced the SNR of the reconstructed images and degraded the accuracy of phase recovery [30]. In addition, minor fluctuations in laser power and the inherent characteristics of the SPI reconstruction process caused frame-to-frame variations in the brightness and contrast of the phase-shifted fringe sequence. These inconsistencies led to significant periodic errors in the phase image, severely degrading 3D reconstruction accuracy.

To enhance the SNR of the reconstructed phase images, a preprocessing workflow was used to each SPI-reconstructed image. This workflow was specifically designed to reduce speckle noise, correct non-uniform fringe amplitudes, and stabilize inter-frame brightness and contrast fluctuations. Specifically, histogram equalization was first applied to ensure consistent contrast and amplitude across the fringe image sequence. Subsequently, a 2D Gaussian low-pass filter (σ = 3 pixels, kernel size = 5 $\times$ 5) was used to reduce noise while preserving the essential fringe structures.

The effectiveness of the proposed preprocessing method was illustrated in Figure 7. In the intensity profiles in Figure 7g,h,i,k,l, the blue, yellow, green, and red curves represented the cross-sections of the four-step phase-shifting fringe patterns, respectively. As shown in Figure 7a, the ideal fringe patterns exhibited smooth intensity distributions. After adding speckle noise and contrast variations, the fringe patterns in Figure 7b became degraded, and the corresponding intensity profiles in Figure 7g showed inconsistencies among different phase steps. As a result, the RMSE of the phase error reached 0.5687 rad.

After applying histogram equalization, the fringe contrast was improved as shown in Figure 7c. The corresponding intensity profiles indicated that the fluctuations were reduced, and the RMSE decreased to 0.1903 rad in Figure 7h. By further applying Gaussian filtering, the fringe patterns became smoother in Figure 7d, and the intensity profiles showed reduced high-frequency fluctuations in Figure 7i. Accordingly, the RMSE was further reduced to 0.1003 rad.

Figure 7j compared the phase error profiles at different processing stages. The blue, yellow, and orange curves corresponded to the unprocessed, histogram equalized, and fully preprocessed results, respectively. Among these, the fully preprocessed result yielded the smallest phase error.

For the experimental results, the SPI reconstructed fringe patterns in Figure 7e contained noticeable noise and intensity distortion, and the corresponding intensity profiles in Figure 7k were less stable. After applying the same preprocessing steps, the fringe patterns in Figure 7f became smoother, and the intensity profiles showed improved consistency in Figure 7l. These results agreed with the simulation results and confirmed the effectiveness of the proposed preprocessing method for SPI fringe reconstruction.

During the measurement phase, the SPI process used a Hadamard matrix derived from the cake-cutting (CC) strategy [31], and the TVAL3 algorithm was used to reconstruct the deformed fringe images from the acquired single-pixel measurements [32]. In the reconstruction, the key TVAL3 parameters were set to μ = 64 and β = 16, while the other

parameters were kept unchanged throughout all experiments. The resulting resolution of the reconstructed images was 128 × 128 pixels. Finally, measurements and analyses were conducted on a step and a standard sphere to quantitatively evaluate the 3D reconstruction accuracy of the proposed system.

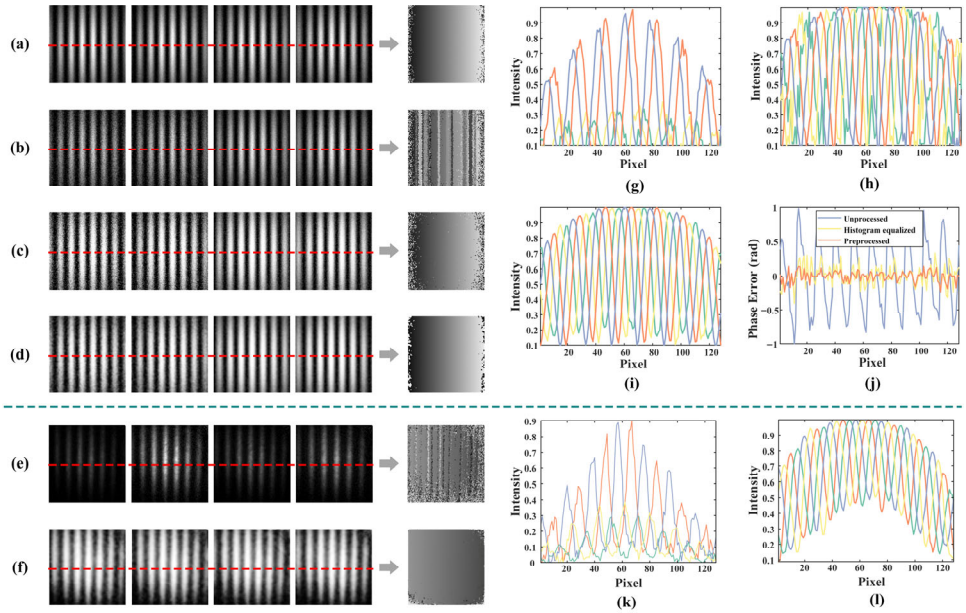


Figure 7. Simulated and SPI reconstructed deformed fringe images before and after preprocessing: (**a**) ideal four-step phase shifted fringe patterns; (**b**) simulated fringe patterns with speckle noise and contrast variations; (**c**) and (**d**) histograms equalized and fully preprocessed images of (**b**), respectively; (**e**) reconstructed fringe patterns by SPI; (**f**) preprocessed images of (**e**); (**g**–**i**) intensity distributions along the red lines marked in (**b**–**d**), respectively; (**j**) phase error profiles of the unprocessed, histogram-equalized, and fully preprocessed results; (**k**) and (**l**) intensity distributions along the red lines marked in (**e**) and (**f**), respectively.

The measurement results for the step were presented in Figure 8. The reconstructed fringe patterns at spatial frequencies of 21, 18, and 16 were shown in Figure 8a–c, respectively. As illustrated by the phase image in Figure 8d, where the absolute phase value corresponding to the red dashed line was indicated, the phase distribution remained continuous with a low noise level, confirming that the reconstructed image quality was sufficient for high-precision phase unwrapping. To evaluate the planar reconstruction accuracy, a plane-fitting analysis was performed on a selected region of the reconstructed point cloud, as shown in the upper panel of Figure 8e. The resulting RMSE of the fitted plane was 1.0239 rad. The heights of the steps were measured to assess the measurement accuracy. The reference heights of the two steps, precisely measured with a micrometer, were 9.98 mm and 9.97 mm. The system measured the corresponding heights as 9.56 mm and 9.35 mm, resulting in measurement errors of 0.42 mm and 0.62 mm, respectively.

Then, a standard sphere with a radius of 25.00 mm was measured to further evaluate the system's accuracy, with the results shown in Figure 9. A spherical fitting algorithm was applied to the reconstructed point cloud data, yielding a fitted radius of 25.0893 mm. The RMSE of the spherical fit was 1.0036 rad. These results demonstrate that the system achieved millimeter-level measurement accuracy under ideal, scatter-free conditions. This baseline performance served as a reliable reference for subsequently evaluating the capability of the system in challenging scattering environments.

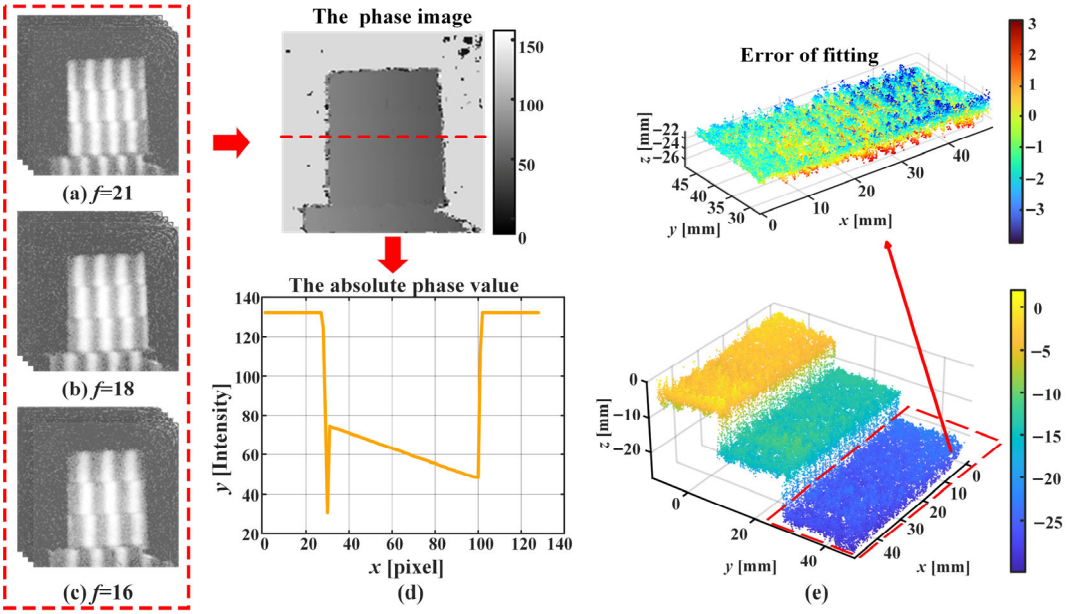


Figure 8. Single-pixel 3D reconstructed point cloud of a step: (**a**–**c**) single-pixel images of the deformed step surface; (**d**) phase distribution; (**e**) 3D point cloud of the step and error analysis of the 3D point cloud.

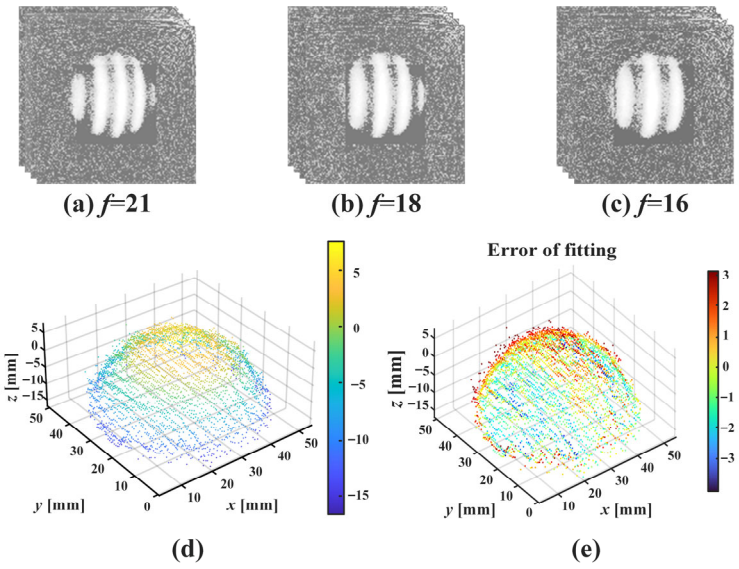


Figure 9. Measurement results of a standard sphere: (**a**–**c**) single-pixel images of the sphere; (**d**) 3D point cloud of the sphere; (**e**) error analysis of the 3D point cloud.

5. System Performance Analysis in Scattering Environments

Since the overall system performance was primarily determined by several key operating parameters [33], this section systematically examined the influence of laser power, DMD projection rate, and SPI encoding mode on the reconstruction quality to identify their optimal combination. The peak signal-to-noise ratio (PSNR) and structural similarity index (SSIM) were used as quantitative evaluation metrics. All metrics were computed within a predefined region of interest (ROI), indicated by the red boxes in the subsequent figures, to prevent noise from irrelevant background regions from affecting the assessment.

5.1. Effect of Laser Power

Water turbidity was fixed at 5 NTU and the DMD projection rate was set to 200 Hz, while the cake-cutting (CC) encoding strategy was adopted. A series of tests were con-

ducted under these conditions to investigate the impact of distinct laser powers and sampling rates on reconstruction quality. The corresponding results were presented in Figure 10. Figure 10a shows the reconstructed phase images at various sampling rates, whereas Figure 10b plots the quantitative variations of the evaluation metrics. Finally, a reference image acquired in clear water (0 NTU) with 140 mW power, 200 Hz rate, and 100% sampling rate was utilized to serve as the ground truth for comparative analysis.

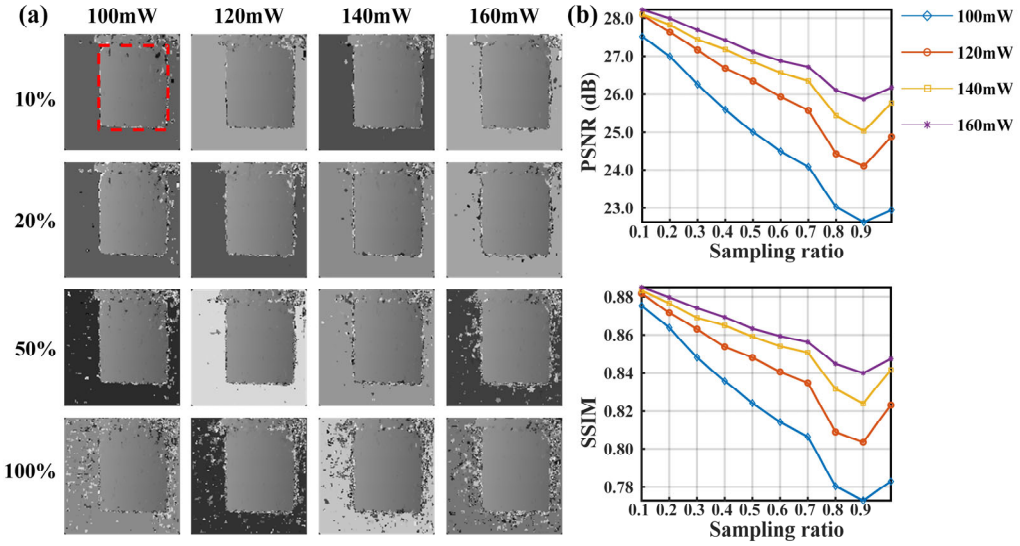


Figure 10. Influence of laser power: (**a**) phase images of the step at different sampling rates; (**b**) evaluation results at different sampling rates.

From the phase images in Figure 10a, it is visually apparent that reconstruction quality was positively correlated with both laser power and sampling rate. Image details become progressively clearer as the sampling rate increases from 10% to 100%. Similarly, increasing the laser power effectively suppressed noise at any given sampling rate. The quantitative results in Figure 10b indicate that higher power performed optimally across almost all metrics by achieving higher PSNR and SSIM, demonstrating its effectiveness in combating water scattering and improving the SNR. It was worth noting that reconstructions at lower sampling ratios sometimes appeared visually smoother than those at full sampling. This occurs because low-ratio sampling primarily captured the dominant low-frequency components of the scene, which naturally reduced noise from environmental scattering. In contrast, full sampling enabled a more complete recovery of fine structural details but also incorporated more noise. As a result, images reconstructed at full sampling exhibited slightly stronger background fluctuations.

On the other hand, the PSNR and SSIM metrics exhibited a decreasing trend as the sampling rate increased. This implies that while a higher sampling rate could better reconstruct the geometry of the object, it simultaneously captured and amplified the noise introduced by water scattering. Comparison against the clear water baseline revealed that this noise difference led to a decrease in the overall image quality metrics.

5.2. Effect of DMD Projection Rate

The projection rate of the DMD was a critical parameter that determined both imaging speed and reconstruction quality. In this experiment, water turbidity was maintained at 5 NTU and laser power was set to 140 mW, while the DMD projection rate was adjusted from 200 Hz to 2000 Hz to investigate its effect. The ground truth was obtained under the same conditions as in Section 5.1.

The phase images in Figure 11a showed the decisive impact of the DMD projection rate. At the lower rate of 200 Hz, the system reconstructed a clear and complete phase image. However, the image quality deteriorated sharply as the projection rate increased. Significant noise began to appear at 400 Hz, and by 800 Hz and above, the image was almost completely overwhelmed by salt-and-pepper noise, with no effective information about the object remaining. The fundamental reason for this phenomenon was that a faster projection rate meant the integration time allocated to the single-pixel detector for each projection pattern became extremely short. In a turbid water environment, where the optical signal was already weak and was filled with scatter, an overly short integration time prevented the detector from collecting sufficient photons. This led to a rapid drop in the SNR, making effective signal reconstruction impossible.

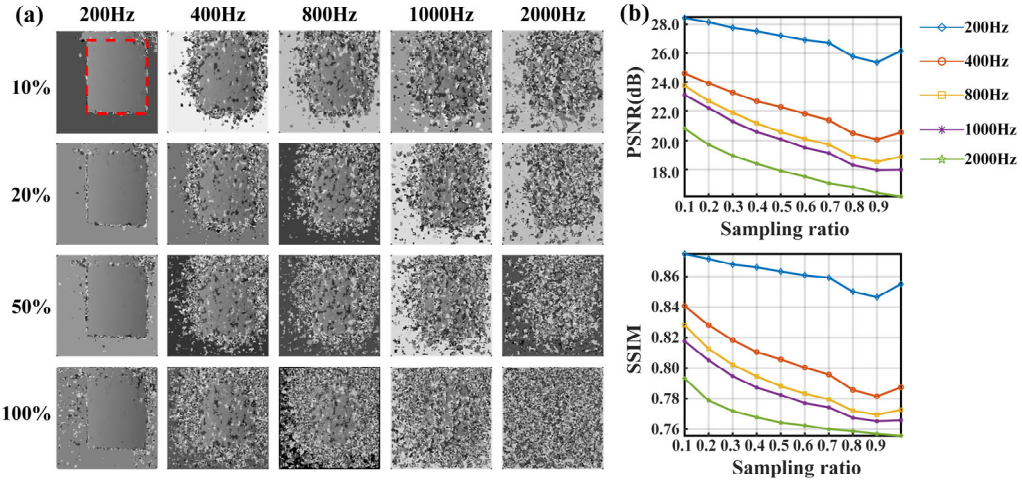


Figure 11. Influence of DMD projection rate: (**a**) phase images of the step at different sampling rates; (**b**) evaluation results at different sampling rates.

In the quantitative analysis of Figure 11b, all image quality metrics showed a strong negative correlation with the projection rate. The curve corresponding to 200 Hz was significantly better than those at other rates in all plots. As the projection rate increased to 400 Hz, 800 Hz, and 2000 Hz, the PSNR and SSIM values plummeted, indicating a severe degradation in the quality of the reconstruction results.

5.3. Comparative Analysis of SPI Encoding Modes

To evaluate the performance of different encoding strategies, this section compared three mainstream SPI modes: FSPI [34], GCS + S [35], and CC. All experiments were carried out under identical conditions, specifically with a laser power of 140 mW and a DMD projection rate of 200 Hz, to ensure a fair comparison. For FSPI, the required sinusoidal basis patterns were binarized using the Bayer dithering algorithm, and a four-step phase shifting method was used to calculate the Fourier coefficients for image reconstruction. For both HSI modes, the TVAL3 algorithm was used to reconstruct the deformed fringe images. The evaluation metrics were calculated using the full-sampling reconstruction result under clear conditions as the ground truth.

The results in Figure 12 show that the FSPI strategy was completely unsuitable within this system. Even in clear water, when the sampling rate was reduced to 10%, the phase image already showed significant noise and structural distortion. As turbidity increased, its performance deteriorated sharply; at 20 NTU, the result at low sampling rates completely failed. These results indicate that the FSPI was less robust to noise than HSI. The fundamental reason was that volume scattering in water produced strong, spatially low-frequency background light noise. Since phase images were recovered by measuring the Fourier

spectrum coefficients of the scene, this low-frequency noise severely contaminated the low-frequency spectral measurements, which contained most of the image energy. Additionally, FSPI required the projection of grayscale sinusoidal fringes; simulating grayscale with a binary dithering algorithm inherently introduced additional noise, further reducing the SNR.

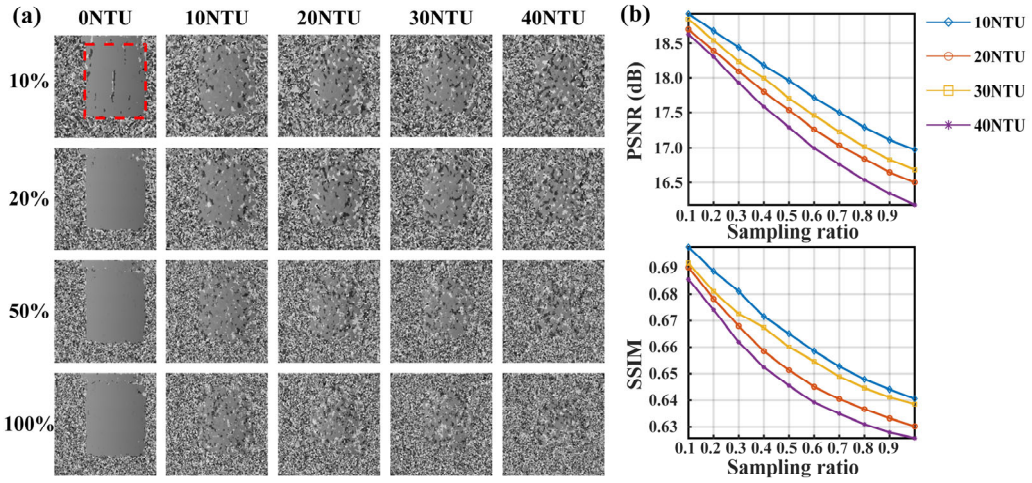


Figure 12. Performance of FSPI strategy under different turbidities: (**a**) phase images of the step at different sampling rates; (**b**) evaluation results at different sampling rates.

In stark contrast to FSPI, the Hadamard basis-based GCS + S and CC strategies demonstrated superior compressive sensing performance, as shown in Figures 13 and 14. Even at a 10% sampling rate and 40 NTU turbidity, both HSI methods successfully reconstructed recognizable object contours in the phase image. This result strongly validated the theoretical advantages of HSI. First, the Hadamard basis was a natural binary orthogonal basis that perfectly matched the binary switching nature of the DMD, thereby avoiding the fidelity loss associated with simulating grayscale in FSPI. Second, the Hadamard transform distributed signal energy across all transform coefficients. When combined with compressive sensing algorithms such as TVAL3, this characteristic enabled the effective differentiation and suppression of spatially correlated noise caused by scattering, demonstrating strong robustness.

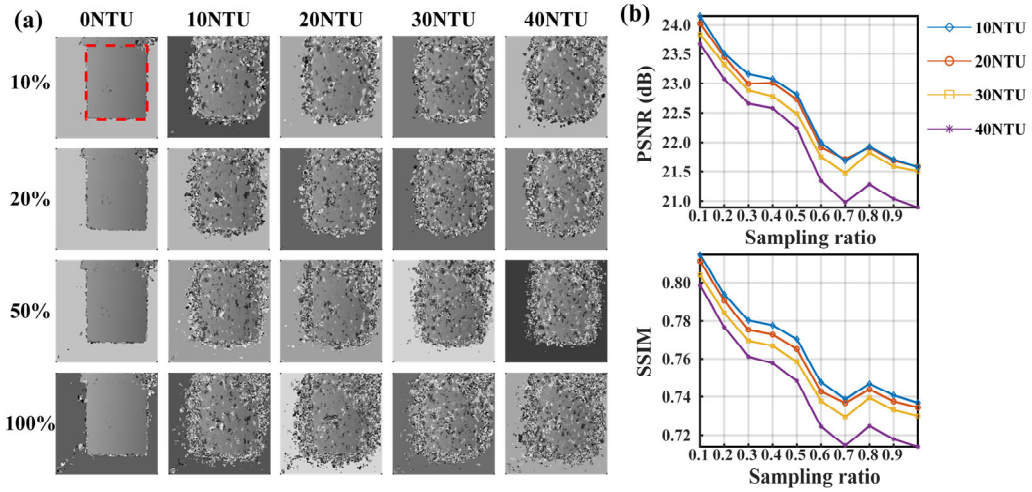


Figure 13. Performance of GCS + S strategy under different turbidities: (**a**) phase images of the step at different sampling rates; (**b**) evaluation results at different sampling rates.

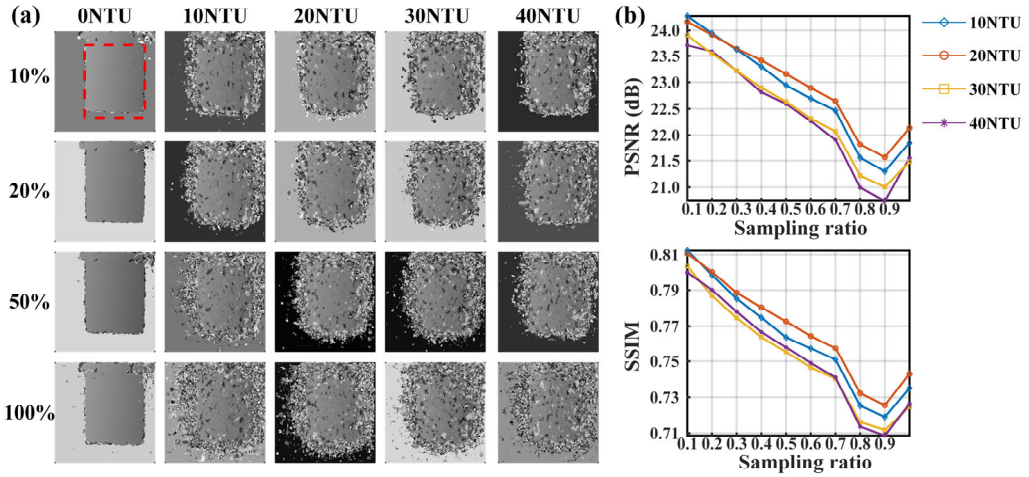


Figure 14. Performance of the CC strategy under different turbidities: (**a**) phase images of the step at different sampling rates; (**b**) evaluation results at different sampling rates.

Tables 1–3 present the mean absolute error (MAE) of the reconstructed phase for different encoding strategies under various scattering levels and sampling rates. It can be seen that the FSPI strategy performed worse than the other two strategies under the tested conditions. In comparison, although the MAE values of CC and GCS + S were very close in some cases, the CC strategy showed better overall performance across different turbidity levels and sampling rates. Therefore, the CC strategy was adopted in this work.

Table 1. MAE of the reconstructed phase for the FSPI strategy with respect to the reference phase.

Rate	Turbidity Levels			
	10 NTU	**20 NTU**	**30 NTU**	**40 NTU**
10%	8.1677	9.5764	9.3839	10.8571
20%	8.3540	9.5360	9.2771	11.0082
50%	8.6522	9.9677	9.8517	11.6064
100%	8.9276	10.1427	9.9083	11.5534

Table 2. MAE of the reconstructed phase for the GCS + S strategy with respect to the reference phase.

Rate	Turbidity Levels			
	10 NTU	**20 NTU**	**30 NTU**	**40 NTU**
10%	3.2688	3.4586	4.3620	4.5494
20%	3.4321	3.7122	4.5370	5.1666
50%	3.4400	3.5329	4.9273	5.2049
100%	3.9441	3.8404	5.8981	6.3344

Table 3. MAE of the reconstructed phase for the CC strategy with respect to the reference phase.

Rate	Turbidity Levels			
	10 NTU	**20 NTU**	**30 NTU**	**40 NTU**
10%	2.7107	3.3974	4.5885	4.9636
20%	2.9794	3.7544	4.5651	4.8274
50%	3.1169	3.6545	4.6370	4.2658
100%	3.2044	3.8166	4.4959	5.3465

According to the preceding system parameter optimization analysis, a near-optimal parameter combination was selected to strike the best balance among reconstruction quality,

speed, and robustness. Specifically, a laser power of 160 mW was chosen as experiments indicated that higher power effectively countered water scattering and significantly improved the SNR. A DMD projection rate of 200 Hz was adopted to ensure that the single-pixel detector maintained sufficient integration time for each encoding pattern to collect weak signals, thereby avoiding signal loss at higher rates. Finally, the CC encoding mode was selected, as it demonstrated more robust absolute phase recovery in scattering environments.

To evaluate the performance of the system in scattering environments, single-pixel 3D reconstruction of a step object was performed under different turbidity levels. Local accuracy was quantified by calculating the plane-fitting RMSE of each step surface, while the global accuracy was evaluated by comparing the reconstructed heights with the ground-truth values. The quantitative results were summarized in Table 4, and showed that although scattering media caused a slight overall increase in surface-fitting error, it remained below 1.4 mm, demonstrating strong robustness in local plane fitting. The absolute error increased gradually from 5.34% at 10 NTU to 6.01% at 40 NTU with a relatively limited increment, indicating that the system could maintain millimeter-level 3D reconstruction accuracy even at high turbidity conditions.

Table 4. Measurement accuracy and plane-fitting errors of the step under different water turbidity levels.

3D Measurements (mm)	Turbidity Levels			
	10 NTU	**20 NTU**	**30 NTU**	**40 NTU**
Height1	9.5335	9.5643	9.4911	9.7068
Height2	9.3514	9.2950	9.3053	9.0439
Absolute error	5.34%	5.47%	5.78%	6.01%
RMSE	1.2738	1.3142	1.3262	1.3489

Overall, these results demonstrated the effectiveness and robustness of the proposed dual-DMD single-pixel 3D imaging system in turbid water environments. They verified that the proposed system could achieve stable and reliable 3D reconstruction under strong scattering conditions.

5.4. Reconstruction of Complex Objects in Scattering Environments

A bionic pufferfish model featuring an intricate surface geometry was selected as the test object to further validate the 3D reconstruction capability of the proposed DSP3DI system in complex scattering environments. The experiments were conducted using the near-optimal parameter combination identified from the performance analysis, as follows: laser power of 160 mW, DMD projection rate of 200 Hz, and a CC encoding mode. Reconstructions were performed under various turbidity and sampling rate conditions, with the results presented in Figure 15.

Under 0 NTU and 100% sampling rate conditions, the system yielded a dense and structurally complete point cloud, accurately reproducing the overall shape of the bionic pufferfish, including its curved body, tail, and fins. Even when the sampling rate was reduced to 10%, the system successfully reconstructed a clearly recognizable object outline, validating the effectiveness of compressive sensing under ideal conditions.

As water turbidity increased, reconstruction quality gradually deteriorated. This degradation was primarily attributed to increased turbidity intensifying light scattering and attenuation, which led to a significant decrease in the effective signal received at the detection end. At 20 NTU, the reconstruction results already exhibited partial data loss. When the turbidity increased to 40 NTU, the reconstructed point cloud became noticeably discontinuous, and much of the fine structural detail was lost. Under the highly turbid

condition of 60 NTU, only the rough outline of the bionic pufferfish could still be recovered. This degradation became even more severe when high turbidity was combined with low sampling rates, because fewer measurements were available for reconstruction under compressed sampling. Consequently, the amount of information proved insufficient to support the reconstruction algorithm, ultimately resulting in reconstruction failure at both 10% and 20% sampling rates.

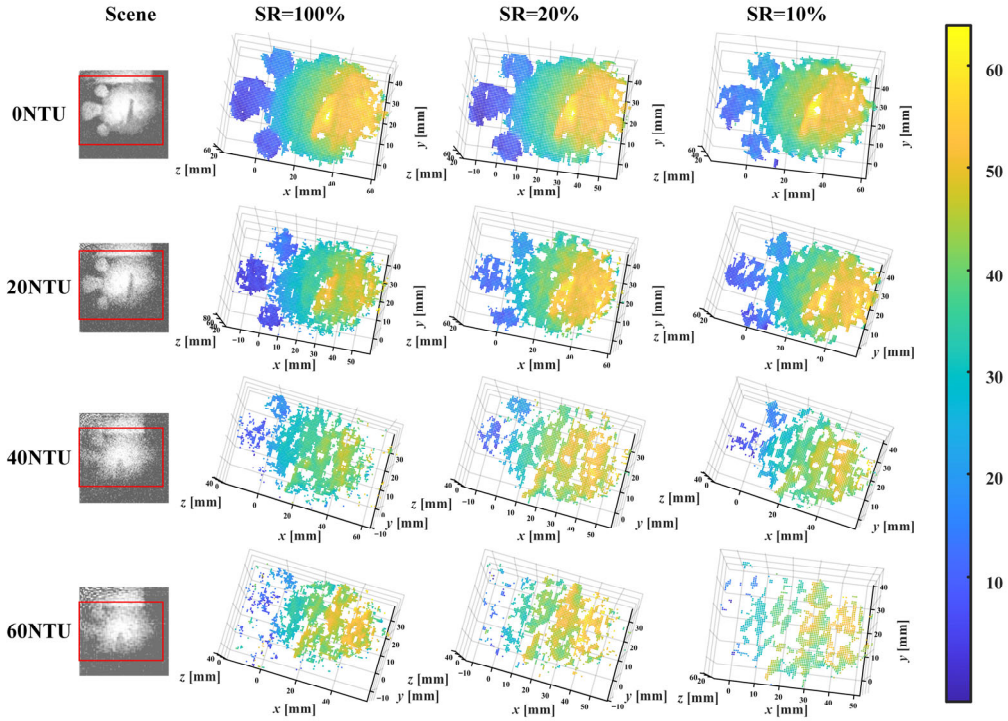


Figure 15. 3D Reconstruction of the bionic pufferfish under different turbidities and sampling rates.

This experiment systematically demonstrated the performance of the DSP3DI system under different turbidity and sampling-rate conditions. In low-turbidity water, the system achieved high-quality 3D reconstruction and maintained good imaging efficiency under compressive sampling. As turbidity increased, the reconstruction performance gradually degraded because of the combined effects of water scattering, target reflectivity, and sampling rate. This degradation was more severe for low-reflectivity objects in highly turbid water and at low sampling ratios. Nevertheless, the ability of the system to still recover the main object shape under challenging conditions demonstrates its robustness and scattering resistance in turbid-water imaging.

6. Discussion

The binarization and preprocessing experiments confirmed the effectiveness of Bayer dithering, histogram equalization, and Gaussian filtering in improving fringe quality and stabilizing phase recovery. The calibration results, together with the measurements of the step and the standard sphere, further supported the ability of the proposed system to establish reliable geometric correspondence and achieve millimeter-level 3D reconstruction accuracy under clear or weak-scattering conditions. More importantly, the experiments in turbid water revealed that the reconstruction quality mainly depended on the received signal strength, which was jointly affected by water scattering, target reflectivity, laser power, DMD projection rate, and sampling ratio. The parameter comparison results further suggested that higher laser power and the CC encoding strategy were more favorable for robust reconstruction, whereas an excessively high projection rate significantly degraded

the reconstruction quality. Accordingly, the reconstruction experiments on representative objects showed that the proposed system could still maintain effective 3D shape recovery under relatively high turbidity and low-sampling-rate conditions.

Compared with previous underwater single-pixel 3D methods, the proposed dual-DMD architecture directly combines DMD-based fringe projection with SPD-based encoded detection, thereby providing a more complete experimental framework for underwater 3D sensing. Nevertheless, the current method is still constrained by weak-signal conditions under strong scattering environments. When the received signal becomes too weak, fine structural details cannot be reliably recovered, and the reconstruction performance degrades accordingly. In addition, the sequential projection and acquisition process still restricts the present system mainly to static or slowly varying scenes. Therefore, further improvements in imaging efficiency and reconstruction robustness are still needed for more challenging practical applications.

7. Conclusions

In this paper, a dual-DMD single-pixel 3D imaging system was designed and constructed to address the challenge that strong scattering effects pose to traditional optical 3D measurement techniques. By integrating binary fringe projection, SPI-based fringe reconstruction, phase retrieval, and pseudo-camera-based geometric calibration, the proposed system achieved effective 3D reconstruction of complex objects in turbid water. Experimental results indicated that the system not only achieves millimeter-level 3D reconstruction accuracy but also performs effective 3D shape reconstruction of objects in highly turbid water, demonstrating its strong scattering resistance and robustness.

Nevertheless, the present system still has several limitations. Its applicability is primarily limited by the received signal level under turbid conditions, which depends on water scattering, target reflectivity, and sampling ratio. When these factors result in excessively weak signals, fine structural details cannot be reliably recovered, leading to significant performance degradation. Future work will focus on improving the overall imaging performance by reducing imaging distortions through more accurate system calibration, distortion compensation algorithms, and optimized optical configuration. In addition, the illumination system will be further enhanced by using higher-power light sources and more efficient structured-light projection schemes to extend the effective imaging distance. With these improvements, the proposed approach is expected to show greater potential for medium- and long-range underwater optical sensing applications, such as underwater archaeology and infrastructure inspection.

Author Contributions: Conceptualization, W.F. and F.Z.; methodology, W.F. and B.W.; software, X.P.; validation, B.W., X.P. and Z.Z.; formal analysis, Z.Z.; investigation, D.T.; resources, W.F. and F.G.; data curation, X.P. and S.L.; writing—original draft preparation, W.F.; writing—review and editing, B.W., F.G. and F.Z.; visualization, Z.Z. and D.T.; supervision, S.L., F.G. and F.Z.; project administration, W.F.; funding acquisition, W.F. All authors have read and agreed to the published version of the manuscript.

Funding: This research was funded by Science and Technology Research Project of Education Department of Hubei Province of China (grant no. D20231406), Yichang Unveiling Technology Project of China (grant no. A24-4-007), and Open Projects funded by Hubei Engineering Research Center for Intelligent Detection and Identification of Complex Parts (grant no. IDICP-KF-2025-08).

Data Availability Statement: The data that support the findings of this study are available from the authors upon reasonable request.

Acknowledgments: Wei Feng gratefully acknowledges the financial support from the China Scholarship Council (CSC) during his academic visit at the Centre for Precision Technologies, University of Huddersfield, United Kingdom.

Conflicts of Interest: The authors declare no conflicts of interest.

Abbreviations

The following abbreviations are used in this manuscript:

BS	Beam splitter
$CaCO_3$	Calcium carbonate
CC	Cake cutting
CCD	Charge-coupled device
CMOS	Complementary metal-oxide-semiconductor
DMD	Digital micromirror device
DSP3DI	Dual-DMD single-pixel 3D imaging
FPP	Fringe projection profilometry
FSPI	Fourier single-pixel imaging
NTU	Nephelometric turbidity unit
PSNR	Peak signal-to-noise ratio
RMSE	Root mean square error
ROI	Region of interest
SNR	Signal-to-noise ratio
SPD	Single-pixel detector
SPI	Single-pixel imaging
SSIM	Structural similarity index measure
TIR	Total internal reflection
TVAL3	Total variation minimization by augmented Lagrangian and alternating direction algorithms

References

1. Fan, X.; Wang, X.; Ni, H.; Xin, Y.; Shi, P. Water-Adapted 3D Gaussian Splatting for Precise Underwater Scene Reconstruction. *Front. Mar. Sci.* **2025**, *12*, 1573612. [CrossRef]
2. Hu, K.; Wang, T.; Shen, C.; Weng, C.; Zhou, F.; Xia, M.; Weng, L. Overview of Underwater 3D Reconstruction Technology Based on Optical Images. *J. Mar. Sci. Eng.* **2023**, *11*, 949. [CrossRef]
3. Thorstensen, J.; Zonetti, S.; Thielemann, J. Light Transport in Turbid Water for 3D Underwater Imaging. *Opt. Express* **2024**, *32*, 45013–45028. [CrossRef]
4. Cao, H.; Jin, X.; Wei, J.; Fan, Y.; Du, D. Diffuse Light Field Imaging through Thick Scattering Media. *Opt. Express* **2025**, *33*, 5147–5161. [CrossRef]
5. Ou, Y.; Fan, J.; Zhou, C.; Tian, S.; Cheng, L.; Tan, M. Binocular Structured Light 3D Reconstruction System for Low-Light Underwater Environments: Design, Modeling, and Laser-Based Calibration. *IEEE Trans. Instrum. Meas.* **2023**, *72*, 5010314. [CrossRef]
6. Hu, J.; An, Q.; Wang, W.; Li, T.; Ma, L.; Yi, S.; Wang, L. Research Progress and Applications of Single-Pixel Imaging Technology. *Photonics* **2025**, *12*, 164. [CrossRef]
7. Li, P.; Zhao, H.; Jiang, W.; Zhang, Z.; Sun, B. A Single-Pixel Imaging Scheme with Obstacle Detection. *Photonics* **2022**, *9*, 253. [CrossRef]
8. Li, Y.; Chen, M.; Qi, J.; Deng, C.; Du, L.; Bo, Z.; Han, C.; Mao, Z.; He, Y.; Shao, X.; et al. Underwater Ghost Imaging with Detection Distance up to 9.3 Attenuation Lengths. *Opt. Express* **2023**, *31*, 38457–38474. [CrossRef] [PubMed]
9. Gao, X.; Zhang, C.; Li, X. Computational Underwater Ghost Imaging Based on Scattering-and-Absorption Degradation. *Opt. Lett.* **2024**, *49*, 4461–4464. [CrossRef]
10. Feng, W.; Yi, Y.; Li, S.; Xiong, Z.; Xie, B.; Zeng, Z. High Turbidity Underwater Single-Pixel Imaging Based on UNet++ and Attention Mechanism at a Low Sampling. *Opt. Commun.* **2024**, *552*, 130106. [CrossRef]
11. Ouyang, Z.; Yu, Z.; Wei, Y.; Wang, D.; Kou, Y.; Li, Y.; Yuan, S.; Zhang, Z.; Zhou, D.; Zhou, X. Single-Pixel Three-Dimensional Imaging Based on 2D Compressed Sensing Algorithm. *Opt. Express* **2025**, *33*, 10442–10453. [CrossRef] [PubMed]

12. Ma, M.; Chen, C.; Fei, H. 3D Single-Pixel Imaging by Virtual Binocular Vision. In Proceedings of the 2024 IEEE International Conference on Industrial Technology (ICIT), Bristol, UK, 6–8 March 2024; pp. 1–4.
13. Aguilar, R.A.P.; Hermosa, N.P.; Soriano, M.N. 3D Fourier Ghost Imaging via Semi-Calibrated Photometric Stereo. *Appl. Opt.* **2021**, *61*, 253–261. [CrossRef] [PubMed]
14. Ma, Y.; Yin, Y.; Jiang, S.; Li, X.; Huang, F.; Sun, B. Single Pixel 3D Imaging with Phase-Shifting Fringe Projection. *Opt. Lasers Eng.* **2021**, *140*, 106532. [CrossRef]
15. Li, T.; Dong, Y.; Wang, X. Fourier Transform Profilometry Using Single-Pixel Detection Based on Two-Dimensional Discrete Cosine Transform. *Opt. Laser Technol.* **2022**, *156*, 108570. [CrossRef]
16. Yang, X.; Jiang, X.; Jiang, P.; Xu, L.; Wu, L.; Hu, J.; Zhang, Y.; Zhang, J.; Zou, B. S2O-FSPI: Fourier Single Pixel Imaging via Sampling Strategy Optimization. *Opt. Laser Technol.* **2023**, *166*, 109651. [CrossRef]
17. Niu, B.; Zhang, F.; Huang, H.; Hao, Z.; Qu, X. High-Precision Single-Pixel 3D Calibration Method Using Pseudo-Phase Matching. *Opt. Express* **2023**, *31*, 9872–9885. [CrossRef]
18. Yang, X.; Liu, Y.; Mou, X.; Hu, T.; Yuan, F.; Cheng, E. Imaging in Turbid Water Based on a Hadamard Single-Pixel Imaging System. *Opt. Express* **2021**, *29*, 12010–12023. [CrossRef]
19. Yang, M.; Wu, Y.; Feng, G. Underwater Environment Laser Ghost Imaging Based on Walsh Speckle Patterns. *Front. Phys.* **2023**, *11*, 1106320. [CrossRef]
20. Lyu, N.; Yu, H.; Han, J.; Zheng, D. Structured Light-Based Underwater 3D Reconstruction Techniques: A Comparative Study. *Opt. Lasers Eng.* **2023**, *161*, 107344. [CrossRef]
21. Feng, W.; Li, S.; Wang, B.; Zhai, Z. High-Turbidity Underwater Fourier Single-Pixel 3D Imaging Based on Pseudo-Camera Calibration with Pixel-Mapping at low Sampling Rates. *Opt. Lasers Eng.* **2025**, *186*, 108737. [CrossRef]
22. Tian, F.; Qin, M.; Lv, N.; Zhao, H.; Nan, Z.; Tao, W. Review of Underwater Laser Imaging Technologies. *Opt. Laser Technol.* **2025**, *192*, 113987. [CrossRef]
23. Fan, H.; Li, S.; Shao, C.; Shen, Y.; Yao, X.-R.; Zhao, Q. Enhanced Fourier Single-Pixel Imaging via Positive-Negative Dithering. *Opt. Lett.* **2025**, *50*, 2247–2250. [CrossRef] [PubMed]
24. Wang, Y.; Zhang, S. Three-Dimensional Shape Measurement with Binary Dithered Patterns. *Appl. Opt.* **2012**, *51*, 6631–6636. [CrossRef] [PubMed]
25. Zhang, S. High-Speed 3D Shape Measurement with Structured Light Methods: A Review. *Opt. Lasers Eng.* **2018**, *106*, 119–131. [CrossRef]
26. Kitchener, B.G.B.; Wainwright, J.; Parsons, A.J. A Review of the Principles of Turbidity Measurement. *Prog. Phys. Geogr.* **2017**, *41*, 620–642. [CrossRef]
27. Wang, F.; Wang, C.; Guan, Q. Single-Shot Fringe Projection Profilometry Based on Deep Learning and Computer Graphics. *Opt. Express* **2021**, *29*, 8024–8040. [CrossRef]
28. Tan, J.; Liu, J.; Wang, X.; He, Z.; Su, W.; Huang, T.; Xie, S. Large Depth Range Binary-Focusing Projection 3D Shape Reconstruction via Unpaired Data Learning. *Opt. Lasers Eng.* **2024**, *181*, 108442. [CrossRef]
29. Liu, Y.; Zhang, B.; Yuan, X.; Lin, J.; Jiang, K. An Improved Projector Calibration Method by Phase Mapping Based on Fringe Projection Profilometry. *Sensors* **2023**, *23*, 1142. [CrossRef]
30. Lv, S.; Kemao, Q. Modeling the Measurement Precision of Fringe Projection Profilometry. *Light Sci. Appl.* **2023**, *12*, 257. [CrossRef] [PubMed]
31. Yu, W.-K. Super Sub-Nyquist Single-Pixel Imaging by Means of Cake-Cutting Hadamard Basis Sort. *Sensors* **2019**, *19*, 4122. [CrossRef]
32. Bian, L.; Suo, J.; Dai, Q.; Chen, F. Experimental Comparison of Single-Pixel Imaging Algorithms. *J. Opt. Soc. Am. A* **2018**, *35*, 78–87. [CrossRef] [PubMed]
33. Chen, Q.; Mathai, A.; Xu, X.; Wang, X. A Study into the Effects of Factors Influencing an Underwater, Single-Pixel Imaging System's Performance. *Photonics* **2019**, *6*, 123. [CrossRef]
34. Zhang, Z.; Ma, X.; Zhong, J. Single-Pixel Imaging by Means of Fourier Spectrum Acquisition. *Nat. Commun.* **2015**, *6*, 6225. [CrossRef]
35. López-García, L.; Cruz-Santos, W.; García-Arellano, A.; Filio-Aguilar, P.; Cisneros-Martínez, J.A.; Ramos-García, R. Efficient Ordering of the Hadamard Basis for Single Pixel Imaging. *Opt. Express* **2022**, *30*, 13714–13732. [CrossRef] [PubMed]

Disclaimer/Publisher's Note: The statements, opinions and data contained in all publications are solely those of the individual author(s) and contributor(s) and not of MDPI and/or the editor(s). MDPI and/or the editor(s) disclaim responsibility for any injury to people or property resulting from any ideas, methods, instructions or products referred to in the content.